Three-dimensional surface displacement of the 2008 May 12 Sichuan earthquake (China) derived from Synthetic Aperture Radar: evidence for rupture on a blind thrust

Marcello de Michele, Daniel Raucoules, Julia de Sigoyer, Manuel Pubellier, Nicolas Chamot-Rooke

Geophysical Journal International

Geophys. J. Int. (2010) **183,** 1097–1103 doi: 10.1111/j.1365-246X.2010.04807.x

Three-dimensional surface displacement of the 2008 May 12 Sichuan earthquake (China) derived from Synthetic Aperture Radar: evidence for rupture on a blind thrust

Marcello de Michele,[1] Daniel Raucoules,[1] Julia de Sigoyer,[2] Manuel Pubellier[3] and Nicolas Chamot-Rooke[3]

[1] *Bureau de Recherches Géologiques et Minières, Natural Risks Division, Orléans, France. E-mail: m.demichele@brgm.fr*
[2] *Laboratoire de Géologie, Ecole Normale Supérieure, Paris, France*
[3] *Laboratoire de Géologie, Ecole Normale Supérieure, UMR* 8538,*CNRS, Paris, France*

Accepted 2010 September 8. Received 2010 September 8; in original form 2010 February 5

SUMMARY

The Sichuan earthquake, *M*w 7.9, struck the Longmen Shan (LMS) range front, China, on 2008 May 12, affecting an area of moderate historical seismicity where little active shortening has been previously reported. Recent studies based on space geodesy have succeeded in retrieving the far field surface displacements caused by the earthquake, but the near field (±25 km from the faults) coseismic surface displacement is still poorly constrained. Thus, shallow fault geometry and shallow coseismic slip are still poorly resolved. Here, for the first time for this earthquake, we combine C and L-band Synthetic Aperture Radar offsets data from ascending and descending tracks to invert for the 3-D surface displacement in the near coseismic field of the Sichuan earthquake. Our data, coupled with a simple elastic dislocation model, provide new results strongly suggesting the presence of a blind thrust striking along the range front and being active at depth during the earthquake. The presence of a rupture on a blind thrust brings new evidence for an out-of-sequence thrusting event and new elements for interpreting the tectonic strain partitioning in the LMS, which has important implications both for seismic hazard assessment and long-term evolution of the mountain belt.

Key words: Satellite geodesy; Seismicity and tectonics; Intra-plate processes.

1 INTRODUCTION

The Longmen Shan (LMS) thrust system bounds the eastern margin of the Tibetan plateau and is considered to be a Triassic transpressive zone that was reactivated during the course of the India–Asia collision (Tapponnier & Molnar 1977; Chen & Wilson 1996; Arne *et al.* 1997; Densmore *et al.* 2007; Godard *et al.* 2009). The LMS front is characterised by a steep topographic gradient displaying a relief of over 5 km within a distance of less than 50 km. Tectonically, the LMS front is a thrust system dominated by three major faults that strike SW–NE (for clarity, we will use nomenclature proposed by Chen & Wilson 1996); from the inner to the outer range, respectively, these are the Wenchuan Fault (WF), the Beichuan Fault (BF) and the Guanxian–Anxian Fault (GF; Fig. 1). The range front displays three principal tectonic units (e.g. Burchfiel *et al.* 2008; Robert *et al.* 2010): a crystalline massif composed of Proterozoic basement and Neoproterozoic cover, a narrow foothills area composed of deformed Paleozoic and Mesozoic sediments and the weakly deformed Sichuan Basin sediments. Recent studies based on thermochronometry across the belt and balanced cross-sections indicate that crustal shortening along a thrust system is responsible for the high topography of the region (Godard *et al.* 2009; Hubbard & Shaw 2009). This process has mainly affected the BF since 10–8 Ma, without substantial activation of the WF.

The Sichuan earthquake ruptured two parallel thrust faults along the LMS front, generating one of the largest seismic ruptures ever documented in a continental thrust event (Dong *et al.* 2008). Field campaigns integrated with seismic profiles indicate that at least two imbricate structures (BF, GF) ruptured during the earthquake (e.g. Liu-Zeng *et al.* 2009; Xu *et al.* 2009). As corroborated by further data interpretation based on synthetic aperture radar (SAR) amplitude images (de Michele *et al.* 2010; Hashimoto *et al.* 2009; Kobayashi *et al.* 2009), BF ruptured over an ∼230 km long segment while GF ruptured over a ∼70 km long segment. Field observations indicate that the slip mechanism was a variable combination of thrust and right lateral displacement. However, the 3-D rupture geometry and the associated surface motion are difficult to measure in the field due to both the inaccessibility of most of the damaged areas and the rapid erosion of the fault scarps. A number of teams worldwide, for instance Hashimoto *et al.* (2010), Shen *et al.* (2009), Hao *et al.* (2009), Kobayashi *et al.* (2009) and Feng *et al.* (2010), have worked with SAR data to partially overcome the difficulties

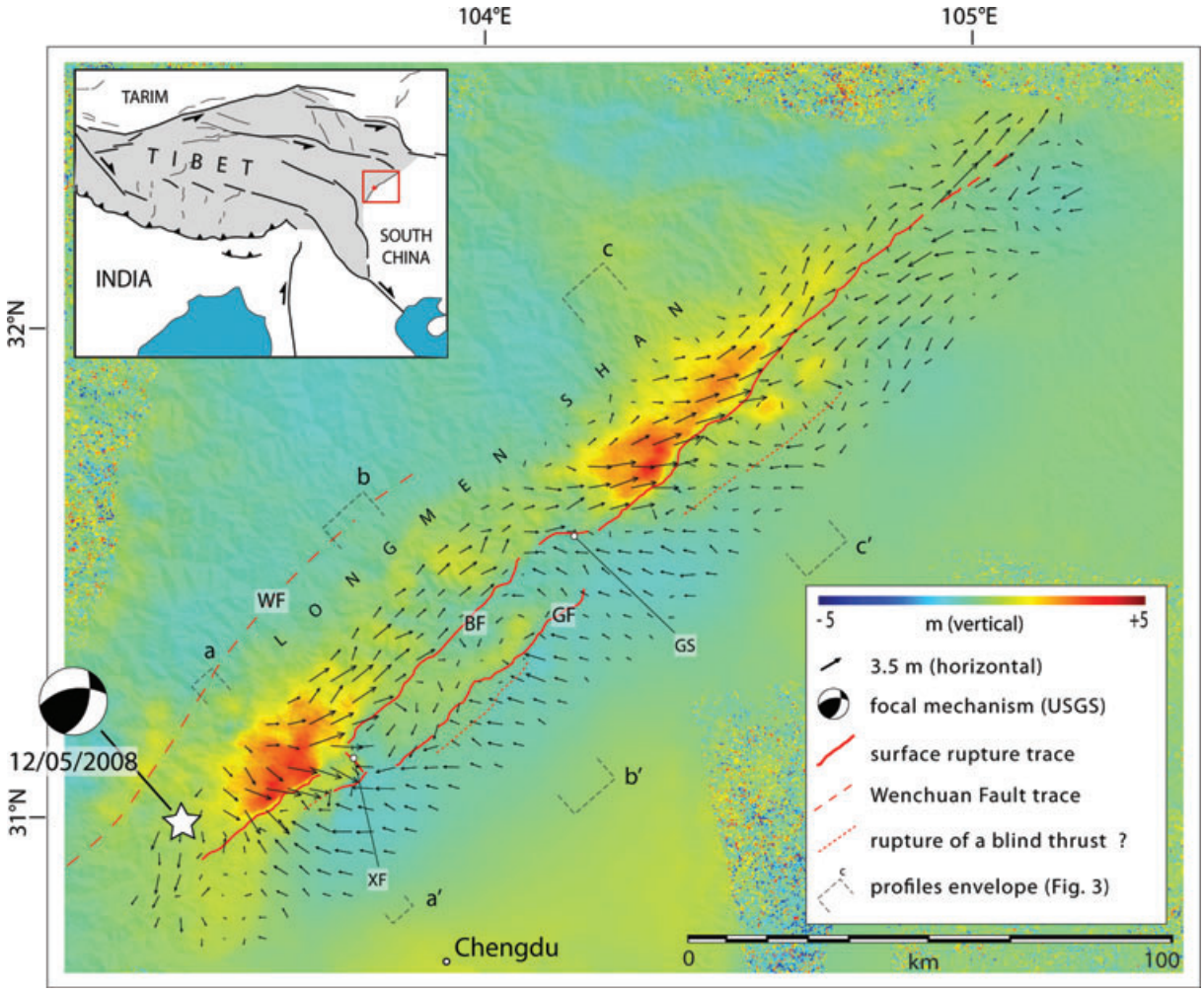

Figure 1. Surface displacement distribution of the Sichuan Earthquake, obtained by SPC of radar amplitude images. Vectors: horizontal displacement components. Colours: vertical displacement components. Surface rupture trace (in plain red) after de Michele *et al.* (2009) and Xu *et al.* (2010). BF, Beichuan Fault; GF, Guanxian–Anxian Fault; WF, Wenchuan Fault; XF, Xiaoyudong Tear Fault; GS, Gaochuan Segment. The background topography (semi-transparent) is the Digital Elevation Model from the Shuttle Radar Topography Mission. Transect locations are shown; aa′, bb′, cc′ represent the stacked profiles envelope.

associated with field data collection. As proposed by Shen *et al.* (2009), Feng *et al.* (2010) and Hao *et al.* (2009), conventional L-band Differential SAR Interferometry (DInSAR) partly overcomes these difficulties by being able to retrieve the surface displacement field from space, in the line-of-sight (LOS) direction of the satellite. Shen *et al.* (2009) used DInSAR and GPS data to retrieve the longer wavelength surface displacement field and used it to constrain a model of coseismic slip distribution on the fault plane at depth. The interferometric phase signals decorrelate quickly close to the seismic rupture, mainly due to the high displacement gradient exceeding the theoretical limit of 1/4 of the wavelength per pixel and the GPS network is too sparse to capture short wavelength surface displacement. Therefore, coseismic surface displacement in the near field is not well resolved. Moreover, ionospheric-related phase delay on the L-band interferograms hampers a unique interpretation of the surface displacement field (Raucoules & de Michele 2009). Feng *et al.* (2010) overcame this problem by carefully choosing SAR couples that are less affected by ionospheric-related phase delay (acquired between 68 and 499 days after the quake). This approach does improve the data quality, but the problem of near-field interferometric phase signal decorrelation still holds.

2 METHODOLOGY

A SAR system sends radar pulses to the ground and measures both the amplitude and the phase of the backscattered signal. Here we use the radar amplitude data to construct ascending and descending correlograms following the subpixel correlation methodology (hereafter named SPC for short) described in Michel *et al.* (1999), which is today a widely used technique for retrieving coseismic surface displacements (e.g. Peltzer *et al.* 2001; Fialko *et al.* 2005). SPC has already been applied to L-band SAR data over the Sichuan earthquake (de Michele *et al.* 2010; Hashimoto *et al.* 2009; Kobayashi *et al.* 2009), but only with ascending data, therefore yielding a non-unique interpretation of the sense of displacement if one does not have *a priori* information on dip angles and slip mechanisms. Here, we use ascending and descending data. To retrieve the 3-D surface displacement in the near field of the earthquake rupture, we use both L-band SAR data from the Japanese Space Agency Phase Array L-band SAR sensor (PALSAR) onboard the ALOS satellite and C-band SAR data from the European Space Agency Advanced-SAR (ASAR) sensor onboard the ENVISAT satellite (Tables 1 and 2).

Table 1. PALSAR data acquisition characteristics.

PALSAR Track	Date	Mode FBS (LOS 34°)	Pixel size Range/ Azimuth (m)
471	2008/02/292008/05/31	Ascending	4.68/3.15
472	2008/01/312008/06/17	Ascending	4.68/3.15
473	2008/02/172008/05/19	Ascending	4.68/3.15
474	2008/04/052008/06/05	Ascending	4.68/3.15
475	2007/12/212008/06/22	Ascending	4.68/3.15
476	2008/04/082008/05/24	Ascending	4.68/3.15

Table 2. ASAR data acquisition characteristics.

ASAR Track	Date	Mode IS2 (LOS 23°)	Pixel size Range/ Azimuth (m)
18	2006/11/152008/05/28	Descending	7.9/3.9
247	2007/11/162008/08/22	Descending	7.9/3.9
290	2008/03/032008/06/16	Descending	7.9/3.9

We have used the following approach; we run the subpixel correlation analysis on the Single Look Complex radar images (SLC) using the correlator implemented in the GAMMA processor (Wegmueller & Werner 1997). First, we compute the correlograms by using a 64 × 128 correlation window size. This provides us with a measurement of the surface displacement that is homogeneous over a cell of ∼300 × 400 m for PALSAR and ∼500 × 500 m for ASAR. We arrange the correlator sampling frequency to provide an independent measurement every ∼64 pixels in the range direction and 128 pixels in the azimuth direction. Secondly, we use the satellite ancillary information to put the correlograms in the original SLC geometry, as specified by the GAMMA correlation procedure (called 'offset tracking'). Thirdly, the correlograms are projected in the DEM geometry (orthorectification).

SPC is less precise than conventional DInSAR interferometry but presents several advantages. C- and L-band correlograms are negligibly sensitive to tropospheric phase delay and are not limited by high surface displacement gradients. Further, we carefully estimated and reduced the ionospheric contribution to the subpixel offset in L-band correlograms using the method described in Raucoules & de Michele (2010).

Each ascending and descending correlogram provides two components of the coseismic offset field, one in the azimuth direction and one in the LOS direction of the satellite, with a precision of up 1/20th of the radar image pixel size (Fig. S1). Thus, we have four non-colinear independent radar observations that we invert to retrieve the east, north and up components of the near-field coseismic surface displacement.

We proceed as follows; let be the unitary vectors associated with the LOS ($u_{r(k)}$) and ($u_{az(k)}$) azimuth directions for each of the two acquisitions (ASAR descending and PALSAR ascending). We use the following rule: the LOS values are positive when we move away from the sensor, azimuth value are positive when acquisition time increases. u_r and u_{az} can be easily defined using the incidence angles and the angles between the orbits and the local meridian. We therefore obtain a four-components data vector:

$$\mathbf{d} = \begin{pmatrix} az_{(1)} \\ az_{(2)} \\ los_{(1)} \\ los_{(2)} \end{pmatrix}$$

az represents the two azimuth offsets and los represents the LOS offsets. Subscripts (1) and (2) refer to the two acquisitions.

From the unitary vectors, we can define a matrix A:

$$\mathbf{A} = \begin{pmatrix} \mathbf{u}^t_{\mathbf{az}(1)} \\ \mathbf{u}^t_{\mathbf{az}(2)} \\ \mathbf{u}^t_{\mathbf{r}(1)} \\ \mathbf{u}^t_{\mathbf{r}(2)} \end{pmatrix}.$$

The relation between the obtained four-components data and the three-components displacement vector is provided by:

$$\mathbf{d} = \mathbf{A}\mathbf{v} \tag{1}$$

$$\mathbf{v} = \begin{pmatrix} \mathbf{dx} \\ \mathbf{dy} \\ \mathbf{dz} \end{pmatrix}$$

is the displacement vector in north, east, up coordinates.

We therefore use a weighted least-squares formulation (e.g. Björk 1996) to derive the displacement vector from the data.

$$\mathbf{V} = (\mathbf{A}^t \mathbf{\Omega} \mathbf{A})\, \mathbf{A}^t \mathbf{\Omega} \mathbf{d}, \tag{2}$$

Ω is the weight matrix, the weights are the signal-to-noise ratio (SNR) values that we estimate during the correlation procedure. For simplicity, we use a diagonal matrix which elements are the SNR correlation values associated to the offset measurement, which allows taking into account the inhomogeneous quality of the measurement.

The results are shown in Fig. 1. We validated our results against field measurements from Xu *et al.* (2009), finding differences with mean ∼0.1 m and standard deviation 0.4 m (Fig. 2), thus showing that SAR provides a reliable estimate of the displacement field from space. The 3-D surface displacement measurements provide us with a unique data set for this earthquake. In particular, we have overcome the need for a direct reliable measurement of the thrust displacement component at the surface—a parameter that is generally difficult to measure in the field.

3 RESULTS

We observed that coseismic displacement along the GF occurred mainly as a thrust movement, whereas the BF underwent more complex motion involving thrusting and dextral displacement, in agreement with previous field observations (Dong *et al.* 2008; Liu-Zeng *et al.* 2009; Xu *et al.* 2009). Three major trends were clearly identified in the displacement field, highlighting a complex strain partitioning. First, in the epicentral area (S-1), surface displacement on BF was accommodated mostly by an oblique thrust mechanism. Average motion on this segment reached ∼3.5 m vertical, ∼3.5 m horizontal-parallel to the fault strike with the dextral slip mechanism and ∼4.8 m horizontal-perpendicular to the fault strike (Fig. 2). No rupture was observed in the field along the SW segment of GF. Nevertheless, transect profiles aa′ (Fig. 3) reveal a small but significant thrust movement close to the southwestern prolongation of GF. Secondly, in the area 30 km northeast of the epicentre (S-2), strain is fully partitioned between BF and GF. Here, surface displacement on BF shows an almost purely dextral strike-slip motion reaching up to ∼3 m. On GF, surface displacement occurs with an almost pure thrust motion, reaching ∼2 m of average vertical displacement and ∼2.3 m of average horizontal displacement. This drastic lateral change in the style of motion reflects differential shortening of the thrust sheets. The differential shortening is associated with the reactivation of the Xiaoyudong tear fault (XF, Fig. 1), a ∼6 km long left-lateral strike-slip boundary between the BF and GF segments. This observation is corroborated by field measurements (Liu-Zeng

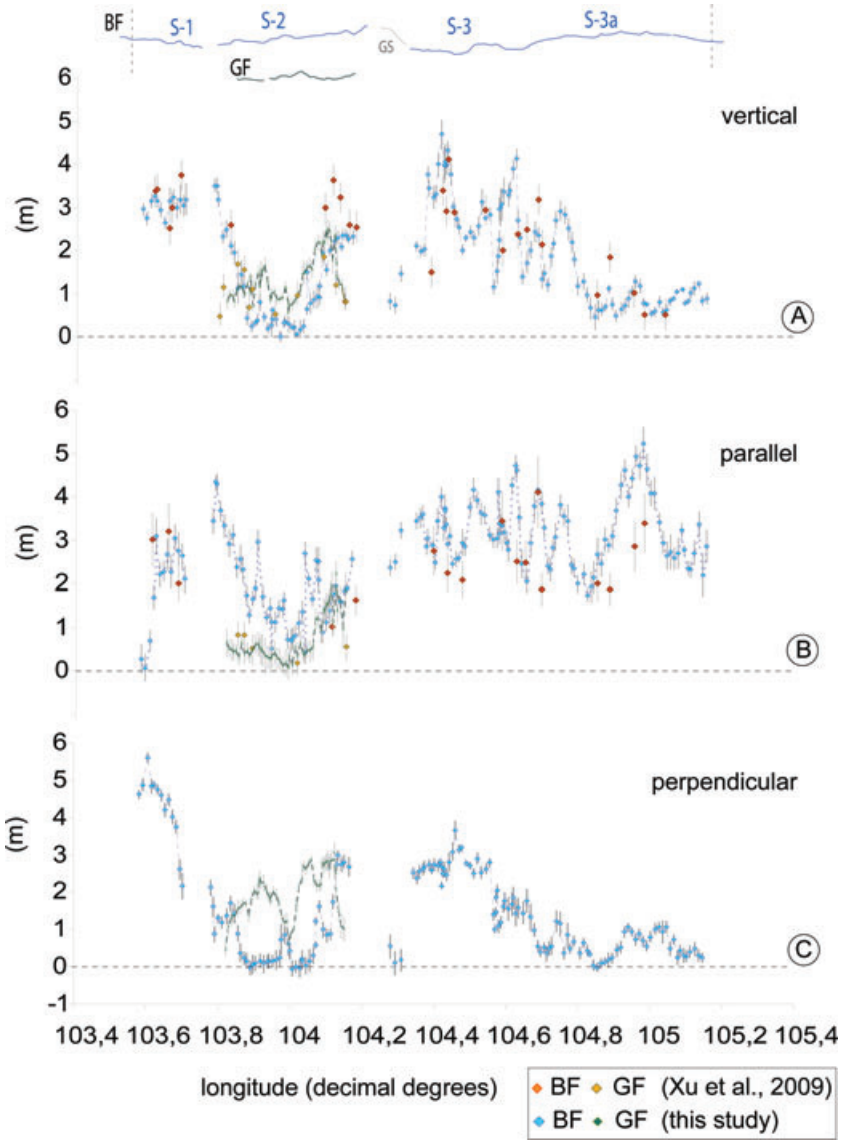

Figure 2. Along-fault-strike evolution of the offset on the BF and GF ruptures as measured by SPC, assuming a ∼N50E fault strike except for GS (the grey segment on top of the figure) whose strike is ∼N80E. Data are sampled every ∼1 km. (a) vertical offset; (b) offset parallel to the fault strike; (c) offset perpendicular to the fault strike. The latter is often extremely difficult to measure in the field. Orange dots: ground measurements from Xu *et al.* (2009) that we averaged over ∼1 km to perform a validation of our radar results.

et al. 2009; Xu *et al.* 2009). Thirdly, in the NE segments on the BF (S-3, S-3a), surface displacement gradually evolves from oblique thrust motion along S-3, with an average displacement of ∼4 m in the vertical and ∼3 m in the horizontal, to almost pure dextral strike-slip motion displaying up to ∼5 m displacement along S-3a, suggesting an evolution from oblique thrust to almost purely dextral strike-slip, consistent with seismological data (Wang *et al.* 2009). **T**he surface rupture occurring on the Gaochuan segment of the BF, between S-2 and S-3, changes strike to ∼N80E for about 11 km (Fig. 1). In our data, we observe that this segment ruptured with oblique dextral motion that is partitioned into strike-slip (∼3 m), vertical (∼1 m) and perpendicular to the fault (∼0.5 m) (Fig. 2).

4 INTERPRETATION AND MODELLING

First, we ask why strain in the LMS system is partitioned between BF and GF in its south–western section and not in its north–eastern section.

While no surface rupture was directly observed in the displacement field along the frontal GF at locations 103°7′ and 104°6′ (Dong *et al.* 2008; Liu-Zeng *et al.* 2009; Xu *et al.* 2009), our transects in Fig. 3 suggest that a small but significant amount of slip at these locations might have occurred at depth on a structure that was activated by the earthquake. As post-seismic displacement can be substantially ruled-out over the period of observation (Shen *et al.* 2009), the pattern of displacement in Fig. 3 would be expected for a coseismic rupture on a blind thrust, possibly at the northern continuation of the GF (Fig. 1) and locally on the SE marginal fault (Chen & Wilson 1996). We verify this hypothesis by comparing the observed data with an elastic dislocation model (Okada 1985) at the locations of transects aa′, bb′, cc′. As our SAR results represent near-field surface displacement measurements (±25 km from the faults), we can resolve the upper crust fault slips and geometry (down to ∼12 km depth). The aim of the modelling is to answer the question of how the newly acquired data modify our previous knowledge. In other words, we wish to show that slip at depth on

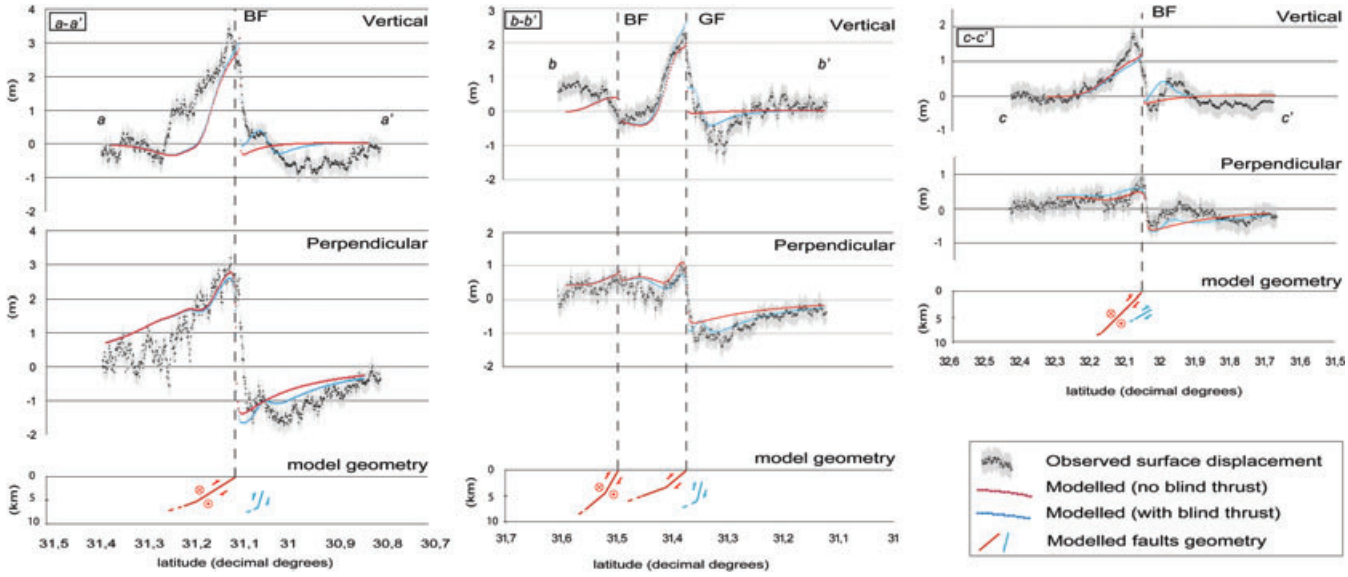

Figure 3. Vertical and perpendicular components across-the-strike of the coseismic surface displacement measured at transect locations aa′, bb′, cc′, versus model results from elastic dislocation modelling. Black dots: radar measurements (with uncertainties); red profile: predicted surface displacement without rupture on a blind thrust; blue profile: predicted surface displacement with rupture on a blind thrust. For each transect, we show the model geometry (refer to the text for the model configuration).

the BF and GF only cannot fully explain the set of observations. We therefore start the modelling procedure with a forward approach. We used the physical theory of Okada (1985), implemented in the code described by Briole *et al.* (1986), for predicting the results of observations. We started with a set of *a priori* information on the geometry and slip of the BF and GF. BF and GF geometry was inferred from the structural models of Jia *et al.* (2010) and Hubbard & Shaw (2009). These models are based on seismic reflection profiles. We also used the mean slip at depth on the BF and GF, as derived in previous works by Hashimoto *et al.* (2010), Shen *et al.* (2009), Hao *et al.* (2009) and Feng *et al.* (2010) who inverted InSAR, GPS and field measurements. In the second step, we used a trial and error approach to explore the model parameters space and slightly adjust the model parameters to ameliorate the fit to the measurements (Table 3). At the end of this step, we noted that the fit to the data in terms of the basic shape of the profile was unsatisfactory. Therefore, we progressed by falsification (e.g. Tarantola 2006). We considered the BF and GF geometry to be fixed and introduced a new fault in the model, representing a rupture on a blind thrust. We tested a number of blind fault geometries. For each model, we compared the predictions to actual observations and rejected models with the highest root-mean-square error (RMSE). Generally, we looked for a model configuration whose prediction jointly best-fit both vertical and horizontal surface displacement observations at transect locations (Table 3, Fig. 3). The blind thrust model parameter space was sampled following Ellis & Densmore (2006) who used elastic dislocation theory to study the evolution of first-order topography in the presence of blind thrusts and their relation to different parameters such as fault dip, fault depth and amount of slip. Once we were satisfied with the forward model configuration, we considered it fixed and inverted for slip only. The inversion is based on the Tarantola–Valette method (Tarantola & Valette 1982) implemented

Table 3. Elastic dislocation model parameters.

	Dip	Length; width (km)	Depth of the fault top edge (km)[a]	E–N (km)[b]	Slip (mm)
Segments (aa′)					
BF (1)	32°	50; 10	0.1	369.437; 3441.742	6120 r
BF (2)	20°	50; 3	5.29	361.437; 3449.742	2300 r
Bt	70°	40; 4	2.8	373.837; 3437.342	2430 r
Segments (bb′)					
BF (1)	60°	64; 5	0.2	403.275; 3480.488	820 r; 3120 ds
BF (2)	40°	64; 5	4.33	401.507; 3482.255	800 r; 3000 ds
GF (1)	40°	40; 5	0.1	411.689; 3470.074	2900 r
GF (2)	20°	40; 5	3.21	410.981; 3472.781	2500 r
Bt	70°	30; 4	2	414.475; 3469.288	2700 r
Segments (cc′)					
BF (1)	45°	70; 19	0.1	461.566; 3543.533	2100 r; 2100 ds
Bt	30°	50; 6	5	464.204; 3536.441	2300 r

Note: Bt, Blind thrust; r, reverse motion; ds, dextral strike-slip motion.
[a]Vertical depth of the segment top edge.
[b]East and North coordinates are in UTM zone 48 and refer to the middle point of the top edge of the fault segment.

in the code inverse 5 described by Briole *et al.* (1986). The inversion was run against two end-member models, with and without blind thrust. We estimated the discrepancy between the model results and the observations by defining an error percentage calculated using the formula described by Battaglia *et al.* (2005) and also by calculating the RMSE. By adding a buried fault in the dislocation model, the percentage error decreased from 53.8 to 41.7, corresponding to an improvement in the RMSE from 0.43 m to 0.29 m.

5 DISCUSSION AND CONCLUSIONS

The most striking result is that without adding an additional rupture on a blind thrust on the range front, the observed surface displacement cannot be satisfactorily reproduced (Fig. 3). This activated blind structure in the range front in the north-eastern sector possibly coincides with previously mapped Quaternary structures (Chen & Wilson 1996; Jia *et al.* 2010; Robert *et al.* 2010) and may be a north-eastern continuation of the GF. Modelled slip on the blind thrust reaches 2.7 m, which is close to the amount of slip found on the GF. Hence, we suggest that where surface displacement evolves from oblique thrust motion to almost pure strike-slip on the BF, crustal shortening is accommodated both on the GF in the south-western sector and on the blind structure at depth in the north-eastern sector. This structural configuration might give rise to the two push-up like structures found in both the epicentral area as well as in the area northeast of Beichuan Town, where vertical displacement reaches a maximum (the two red patches in Fig. 1). In these two areas, strain is not fully partitioned between the BF and the GF. Therefore, transpressional shortening might be accompanied by vertical thickening. Partitioning of transpressional strain can occur when stress is applied oblique to pre-existing structures (e.g. Jones & Tunner 1995). On a larger picture, we observe that the displacement field recorded during the Sichuan earthquake is compatible with oblique stress applied to inherited $\sim$N50° oriented thrust faults within an overall ENE–WSW compression, as also suggested by the maximum horizontal stress derived from nearby drilling observations in the Sichuan basin (Heidbach *et al.* 2007) and the work of Liu-Zeng *et al.* (2009). Although there are certainly blind structures in the Sichuan basin, very little is known about them (e.g. Jia *et al.* 2009). A good statistical fit does not guarantee a good, or even a reasonable, description of reality. Our model rather represents one solution that cannot be disregarded. This solution strengthens the hypothesis of a blind rupture at depth on the range front and provides a new argument in favour of an out-of-sequence thrusting event (Morley 1988), as first proposed by Liu-Zeng *et al.* (2009), for the LMS. This result calls for further investigation of the seismic activity on hinterland to marginal thrusts, which have a twofold importance: for understanding the long-term evolution of the mountain belt and for reassessing seismic hazard in the area.

ACKNOWLEDGMENTS

SAR data were provided by JAXA and ESA through the French CIEST agreement (Cellule d'Intervention et d'Expertise Scientifique et Technique) and the International Charter on Space and Major Disasters. We are thankful to Cecile Lasserre, Yann Klinger and Jerome van der Woerd for constructive comments, and to Pierre Briole for his advice on the elastic dislocation model.

REFERENCES

Arne, D., Worley, B., Wilson, C., Chen, S.F., Foster, D., Luo, Z.L., Liu, S.G. & Dirks, P., 1997. Differential exhumation in response to episodic thrusting along the eastern margin of the Tibetan Plateau, *Tectonophysics,* **280,** 239–256.

Battaglia, J., Aki, K. & Ferrazzini, V., 2005. Location of tremor sources and estimation of lava output using tremor source amplitude on the Piton de la Fournaise volcano: 1. location of tremor sources, *J. Volc. Geotherm. Res.,* **147**(3–4), 268–290.

Björck, Åke, 1996. *Numerical Methods for Least Squares Problems,* SIAM, Philadelphia.

Briole, P., De Natale, G., Gaulon, R., Pingue, F. & Scarpa, R., 1986. Inversion of geodetic data and seismicity associated with the Friuli earthquake sequence (1976–1977) Italy, *Ann. Geophys.,* **4B,** 481–492.

Burchfiel, B.C. *et al*., 2008. A geological and geophysical context for the Wenchuan earthquake of 12 May 2008, Sichuan, People's Republic of China, *GSA Today,* **18,** 4–11.

Chen, S.F. & Wilson, C.J.L., 1996. Emplacement of the Longmen Shan Thrust-Nappe belt along the eastern margin of the Tibetan plateau, *J. Struct. Geol.,* **18,** 413–430.

de Michele, M., Raucoules, D., Lasserre, C., Pathier, E., Klinger, Y., Van Der Woerd, J., de Sigoyer, J. & Xu, X., 2010. The *M*w 7.9, 12 May 2008 Sichuan earthquake rupture measured by sub-pixel correlation of ALOS PALSAR amplitude images, *Earth Planets Space*, in press, doi:10.5047/eps.2009.05.002.

Densmore, A.L., Ellis, M.A., Li Yong, Zhou Rongjun, Hancock, G. S. & Richardson, N., 2007. Active tectonics of the Beichuan and Pengguan faults at the eastern margin of the Tibetan Plateau, *Tectonics,* **26,** doi:10.1029/2006TC001987.

Dong, Sh.W. *et al*., 2008. Surface rupture and co-seismic displacement produced by the Ms 8.0 Wenchuan earthquake of May 12th, 2008, Sichuan, China: eastward growth of the Qinghai-Tibet Plateau, *Acta Geol. Sin. (English Version),* **82,** 938–948.

Ellis, M.A. & Densmore, A.L., 2006. First order topography over blind thrusts, *GSA Special Papers,* **398,** 251–266, doi:10.1130/2006.2398(15).

Feng, G., Hetland, A.E., Ding, X., Li, Z. & Zhang, L., 2010. Coseismic fault slip of the 2008 Mw 7.9 Wenchuan earthquake estimated from InSAR and GPS measurements, *Geophys. Res. Lett.,* **37,** L01302, doi:10.1029/2009GL041213.

Fialko, Y., Sandwell, D., Simons, M. & Rosen, P., 2005. Three-dimensional deformation caused by the Bam, Iran, earthquake and the origin of shallow slip deficit, *Nature,* **435,** 19, doi:10.1038/nature03425.

Godard, V., Pik, R., Lavé, J., Cattin, R., Tibari, B., de Sigoyer, J., Pubellier, M. & Zhu, J., 2009. Late Cenozoic evolution of the central Longmen Shan, eastern Tibet: Insight from (U-Th)/He thermochronometry, *Tectonics,* **28,** TC5009, doi:10.1029/2008TC002407.

Hao, K.X., Si, H., Fujiwara, H. & Ozawa, T., 2009. Coseismic surface-ruptures and crustal deformations of the 2008 Wenchuan earthquake Mw7.9, China, *Geophys. Res. Lett.,* **36,** L11303, doi:10.1029/2009GL037971.

Hashimoto, M., Enomoto, M. & Fukushima, Y., 2010. Coseismic Deformation from the 2008 Wenchuan, China, Earthquake Derived from ALOS/PALSAR Images, *Tectonophysics,* **491,** 59–71, doi:10.1016/j.tecto.2009.08.034.

Heidbach, O., Fuchs, K., Müller, B., Renecker, J., Sperner, B., Tingay, M. & Wenzel, F., 2007. *The World Stress Map – Release 2005*, 1:46,000,000, Commision of the World ed., Paris.

Hubbard, J. & Shaw, J.H., 2009. Uplift of the Longmen Shan and Tibetan plateau and the 2008 Wenchuan (M = 7.9) earthquake, *Nature,* **458,** 94–197.

Jia, D. *et al.*, 2010. Structural model of 2008 *M*w7.9 Wenchuan earthquake in the rejuvenated Longmen Shan thrust belt, China, *Tectonophysics,* **491,** 174–184.

Jones R. & Tunner, P.W.G., 1995. Strain partitioning in transpression zones, *J. Struct. Geol.,* **17**(6), 793–802.

Kobayashi, T., Takada, Y., Furuya, M. & Murakami, M., 2009. Locations and types of ruptures involved in the 2008 Sichuan earthquake inferred from SAR image matching, *Geophys. Res. Lett.,* **36**, L07302, doi:10.1029/2008GL036907.

Liu-Zeng, J. *et al*., 2009. Co-seismic ruptures of the 12 May 2008, Ms 8.0 Wenchuan earthquake, Sichuan: east-west crustal shortening on oblique,

parallel thrusts along the eastern edge of Tibet, *Earth planet. Sci. Lett.,* **286,** 355–370, doi:10.1016/j.epsl.2009.07.017.

Michel, R., Avouac J.P. & Taboury J., 1999. Measuring ground displacements from SAR amplitude images: application to the Landers earthquake, *Geophys. Res. Lett.,* **26,** 875–878.

Morley, C.K., 1988. Out of Sequence Thrusts, *Tectonics,* **7**(3), 539–561.

Okada, Y., 1985. Surface deformation due to shear and tensile faults in a half space, *Bull. seism. Soc. Am.,* **75,** 1135–1154.

Peltzer, G., Crampé, F. & Rosen, P., 2001. The *M*w7.1, Hector Mine, California earthquake: surface rupture, surface displacement field, and fault slip solution from ERS SAR data, *C. R. Acad. Sci. Paris,* **333,** 545–555.

Raucoules D. & de Michele, M., 2010. Assessing ionospheric influence on L-band SAR data: implications on co-seismic displacement measurements of the 2008 Sichuan Earthquake, *Geosci. Remote Sens. Lett.,* **7**(2), 286–290, doi:10.1109/LGRS.2009.2033317.

Robert, A., Pubellier, M., de Sigoyer, J., Lahfid, A., Cattin, R., Findling, N. & Zhu, J., 2010. Structural and thermal characters of the Longmen Shan (Sichuan, China), *Tectonophysics,* **491,** 165–173, doi:10.1016/j.tecto.2010.03.018.

Shen, Z.-K. *et al*., 2009. Slip maxima at fault junctions and rupturing of barriers during the 2008 Wenchuan earthquake, *Nature Geosci.,* **2,** 718–724, doi:10.1038/NGEO636.

Tapponnier, P. & Molnar, P., 1977. Active faulting and tectonics in China, *J. geophys. Res.,* **82**(B20), 2905–2930.

Tarantola, A., 2006. Popper, Bayes and the inverse problem, *Nature Phys.,* **2,** 492–494.

Tarantola, A. & Valette, B., 1982. Inverse problems = quest for information, *J. Geophys.,* **50,** 159–170.

Wang, Z., Fukao, Y. & Pei, S., 2009. Structural control of rupturing of the Mw7.9 2008 Wenchuan Earthquake, China, *Earth planet. Sci. Lett.,* **279,** 131–138, doi:10.1016/j.epsl.2008.12.038.

Wegmüller, U. & Werner, C. L., 1997. GAMMA SAR processor and interferometry Software, in *Proceedings of the 3rd ERS Scientific Symposium,* Florence, Italy, 1997 March 17–20.

Xu, X., Wen, X., Yu, G., Chen, G., Klinger, Y., Hubbard, J. & Shaw, J., 2009. Coseismic reverse- and oblique-slip surface faulting generated by the 2008 Mw 7.9 Wenchuan earthquake, China, *Geology,* **37**(6), 515–518.

SUPPORTING INFORMATION

Additional Supporting Information may be found in the online version of this article:

Figure S1. Correlograms used to retrieve the 3-D displacement field. (A) PALSAR LOS SPC offsets, (B) PALSAR azimuth offset (after de Michele *et al.* 2009); (C) ASAR LOS offsets, (D) ASAR azimuth offset (for the acquisition dates, please refer to Tables 1 and 2 in the text).

Please note: Wiley-Blackwell are not responsible for the content or functionality of any supporting materials supplied by the authors. Any queries (other than missing material) should be directed to the corresponding author for the article.